REPORT DOCUMENTATION PAGE

AFRL-SR-BL-TR-01-

0316

1. AGENCY USE ONLY *(Leave blank)*	2. REPORT DATE	3. REPORT
	05/01/01	FINAL REPORT: 01NOV 99 TO 31 OCT 00

4. TITLE AND SUBTITLE
INTERACTION BETWEEN NEAR-WALL TURBULENT FLOWS AND COMPLAINT SURFACES

5. FUNDING NUMBERS
F49620-00-1-0029

6. AUTHOR(S)
JOHN LUMLEY AND DIETMAR REMPFER

7. PERFORMING ORGANIZATION NAME(S) AND ADDRESS(ES)
SIBLEY SCHOOL OF MECHANICAL & AEROSPACE ENGINEERING
CORNELL UNIVERSITY
ITHACA NY 14853

8. PERFORMING ORGANIZATION REPORT NUMBER

9. SPONSORING/MONITORING AGENCY NAME(S) AND ADDRESS(ES)
AFOSR/NA
801 N. RANDOLPH ST.
ARLINGTON VA 22203

10. SPONSORING/MONITORING AGENCY REPORT NUMBER

11. SUPPLEMENTARY NOTES

AIR FORCE OFFICE OF SCIENTIFIC RESEARCH (AFOSR)
NOTICE OF TRANSMITTAL DTIC THIS TECHNICAL REPORT
HAS BEEN REVIEWED AND IS APPROVED FOR PUBLIC RELEASE
LAW AFR 190-12. DISTRIBUTION IS UNLIMITED.

12a. DISTRIBUTION AVAILABILITY STATEMENT

CLEARED FOR PUBLIC DISTRIBUTION

13. ABSTRACT *(Maximum 200 words)*

THE GENERAL AIM OF THIS PROJECT IS TO GET AN IMPROVED UNDERSTANDING OF THE INTERACTION BETWEEN WALL-GENERATED TURBULENCE AND COMPLIANT SURFACE COATING USING ANALYSIS AND DIRECT NUMERICAL SIMULATION IN AN INTEGRATED APPROACH, WITH A VIEW TOWARDS THE REDUCTION OF TURBULENT SOUND PRODUCTION AND TURBULENT DRAG.

20010508 055

14. SUBJECT TERMS
INTERACTION, NEAR-WALL TURBULENT FLOWS AND COMPLIANT SURFACES

15. NUMBER OF PAGES

16. PRICE CODE

17. SECURITY CLASSIFICATION OF REPORT	18. SECURITY CLASSIFICATION OF THIS PAGE	19. SECURITY CLASSIFICATION OF ABSTRACT	20. LIMITATION OF ABSTRACT
UNCLASSIFIED	UNCLASSIFIED	UNCLASSIFIED	UL

Interaction between Near-Wall Turbulent Flows and Compliant Surfaces

John Lumley and Dietmar Rempfer

Sibley School of Mechanical &
Aerospace Engineering
Cornell University
Ithaca, NY 14853
Email(JL): jll4@cornell.edu
Email(DR): dr36@cornell.edu

Grant Number: F49620-00-1-0029

Final Report

April 23, 2001

Abstract

The general aim of this project is to get an improved understanding of the interaction between wall-generated turbulence and compliant surface coatings using analysis and direct numerical simulation in an integrated approach, with a view towards the reduction of turbulent sound production and turbulent drag.

For this purpose, in a first step that is targeted at identifying interesting domains in the space of parameters describing properties of a compliant wall coating, we are developing low-dimensional models based on Galerkin projection of the Navier-Stokes equations onto systems of eigenfunctions obtained via Proper Orthogonal Decomposition. Because of the relatively small effort involved in simulating and analyzing such models, this will allow us to scan large regions of parameter space, allowing us to find regions that lead to a reduction of turbulent drag and turbulent sound production.

Among the ultimate goals of this project are thus, first, to obtain a fundamental understanding of flow-structure interaction phenomena for the case of the compliant-wall/turbulence interaction, and second, to use this understanding to enhance the flight performance of air vehicles by increasing their lift-to-drag ratio.

1 Statement of Objectives

In this study, research is conducted into the issue of the interaction between a turbulent boundary layer and an adjacent compliant surface. This work has as one of its main objectives an improved understanding of the dynamical mechanisms at work in such a situation. Ultimately, this understanding then will be used to manipulate the turbulent flow such that some of its characteristics are altered in a desirable way. In this respect, we are mostly interested in two goals. We want to be able to reduce the turbulent drag generated by such boundary layers, and we also want to be able to attenuate the noise that is generated by the turbulent flow.

In order to achieve this, we will try to find regions in the space of parameters describing mechanical properties of compliant coatings (stiffness, damping) within which the interaction between the wall and the turbulent flow is such that the above goals can be achieved.

The research proposed here consists of two main components. To be able to determine regions in the parameter space of the wall coating that are of interest, we will construct low-dimensional models based on Galerkin projections onto Karhunen-Loève eigenfunctions. These models can only approximately describe the dynamics of the turbulent flow, but because of their low-dimensionality, they allow us to look at large regions of the parameter space. Once promising combinations of parameters are determined, we will then use accurate direct numerical simulations to assess the interaction between turbulence and the compliant wall in more detail.

2 Status of Effort

Our work on developing and incorporating models for the interaction between the turbulent flow and the compliant wall is proceeding as planned. We have developed a refined low-dimensional model, that removes many of the limitations of the previous one, results of which were reported in our previous report. In parallel, we have been working on a computer code for the direct numerical simulation of turbulence/compliant-wall interaction. Results from numerical simulations performed with that code are also presented below.

3 Accomplishments

3.1 Introduction

We start this section with a discussion of the approximations and assumptions that go in a particular low-dimensional model that is described below. We will first present an order-of-magnitude analysis of the boundary condition, and then develop an implementation of the boundary condition in the pressure term under general conditions. It will be shown that for our case, as a reasonable approximation one can model a wall that moves in the wall-normal coordinate only, which allows us to deal with non-zero velocity boundary conditions for the

wall-normal and streamwise coordinate only. We will also derive the coupling coefficient between the wall motion and the fluid mechanics that appears as an additional term in the equation for the wall-normal velocity component. The net result of this analysis suggests that for the purposes of our low-dimensional model, neglect of the nonlinear terms in the boundary conditions is usually quite justifiable.

3.2 Construction of a Low-Dimensional Model for the Wall-Flow Interaction

In this section we will introduce the dynamical model we have developed for describing the behavior of near-wall turbulence over a compliant boundary. The dynamical equations are obtained from:

- Galerkin projection of the Navier-Stokes equations onto a special set of basis functions. In order to capture as much of the dynamics of the flow in a set of modes that is as small as possible, we are using Karhunen-Loève eigenfunctions (derived from a rigid-wall turbulent flow), which are complemented by Stokes eigenfunctions in order to be able to account for the compliant-wall boundary condition.

- The assumption that the compliant wall can be modeled as a simple damped mass-spring system. This means that the type of wall-coating we have in mind can be envisioned as some sort of a thin rubber layer, and it will become clear below that we are also assuming the deformations of the wall to be small. These assumptions are compatible with the results reported in [3]. The deformation of the wall is driven by pressure fluctuations (for the wall normal deformations), and by the fluctuating wall shear for tangential deformations of the wall.

3.2.1 Flow Equations

For these preliminary calculations, we are constructing a model that is analogous to the one first presented by Aubry *et al.* [1], which is also described in much greater detail in the monograph by Holmes, Lumley & Berkooz [5]. This means in particular that we are dealing with streamwise-invariant modes only, arguing that these modes should dominate the behavior of our flow just as they have been demonstrated to do in the rigid-wall case. Thus, we are going to represent our flow fields using a decomposition of the form

$$\tilde{\boldsymbol{u}}(y,z,t) = \boldsymbol{U}(y) + \sum_{j,k} a^{(j,k)} \boldsymbol{\varphi}^{(j,k)}(y) \mathrm{e}^{\mathrm{i}kz} + \text{c.c.}, \tag{1}$$

where y and z are the spanwise and wall-normal coordinates, respectively, k is the spanwise wave number, and j denotes the order of the basis function corresponding to a given wave number k. The function $\boldsymbol{\varphi}^{(j,k)}$ is the jth basis function corresponding to wave number k. In the model described below, the index j will assume the values of 1 or 2 only. This means that, as in [1], we will be using just one POD mode per wave number, described

by the function $\boldsymbol{\varphi}^{(1,k)}(y)$. For the second and third mode, $\boldsymbol{\varphi}^{(2/3,k)}(y)$, we will use Stokes eigenfunctions (see below, § 3.2.5). The main role of these Stokes functions will be to allow us to match non-zero velocity boundary conditions at the wall, which are necessary for a moving wall (remember that the $\boldsymbol{\varphi}^{(1,k)}(y)$ are POD modes from a rigid-wall case, which have $\boldsymbol{\varphi}^{(1,k)}(y=0)=0$). The Stokes functions are chosen such that they are orthogonal to the Karhunen-Loève modes, so that $(\boldsymbol{\varphi}^{(i,k)}, \boldsymbol{\varphi}^{(j,k)}) = \delta_{ij}$.

With these preparations, the equations for the fixed wall (for each spanwise wavenumber k, and for each "quantum number" j) are of the form [5]

$$\begin{aligned}\dot{a}^{(j,k)} &= \sum_n \left(b_{nk}^{j,\text{meanvel}} + (1+2\pi\alpha) b_{nk}^{j,\text{visc}} \right) a^{(n,k)} \\ &+ \sum_{k',p,q} c^j_{(k',k-k')_{pq}} a^{(p,k')} a^{(q,k-k')} \\ &+ \sum_{n,k',p,q} d^j_{nk'pq} a^{(n,k)} \Re\left(a^{(p,k')} a^{(q,k')*} \right). \end{aligned} \tag{2}$$

Since we are actually interested in dealing not with a fixed but with a deformable wall, the above equations, derived for a fixed wall, are not sufficient to describe that situation, and need to be extended by

- adding equations that describe the new boundary conditions for a moving wall, and
- taking into account the influence of the pressure term at the moving wall.

3.2.2 Boundary Conditions

Our coordinate system is such that the undisturbed compliant surface occupies the plane $y = 0$. Let $\boldsymbol{\xi}(z) = [\xi_1, \xi_2, \xi_3](z)$ be the displacement vector of the compliant surface (remember that we assume streamwise invariance). The correct set of boundary conditions is given by

$$\tilde{u}_i(\boldsymbol{x} + \boldsymbol{\xi}, t) = \dot{\xi}_i, \tag{3}$$

where $\tilde{\boldsymbol{u}}$ is the instantaneous fluid velocity, and $\dot{\boldsymbol{\xi}}$ denotes the time derivative of the wall displacement vector. For our model, we will assume that the surface displacements are small, more specifically, we assume that $|\boldsymbol{\xi}^+| = |\boldsymbol{\xi}| u_\tau/\nu \leq 5$, so that the velocity profiles are linear[1]. Under this assumption, the boundary condition can be linearized, giving

$$\tilde{u}_i(0,z,t) + \tilde{u}_{i,j}(0,z,t)\xi_j(z,t) = \dot{\xi}_i(z,t). \tag{4}$$

If we express the instantaneous fluid velocity in terms of the fluctuating components $u_i(\boldsymbol{x},t)$ and the mean $\boldsymbol{U} = [U_1(y), 0, 0]$,

$$\tilde{u}_i = U_i + u_i, \tag{5}$$

[1]Note that this magnitude of $\boldsymbol{\xi}$ coincides with the findings in [3].

we can write (4) as

$$u_i(0,z,t) + U_{i,j}(0)\xi_j(z,t) + u_{i,j}(0,z,t)\xi_j(z,t) = \dot{\xi}_i(z,t), \tag{6}$$

where we have used $U_i(0) = 0$. Let us now assume that $u_i(0,z,t)$ and $\xi_i(z,t)$ are both small quantities in a sense yet to be defined. Let us consider the velocity gradient tensor at $y = 0$, $u_{i,j}(0,z,t)$. We may write

$$\begin{pmatrix} 0 & u_{1,2} & \underbrace{u_{1,3}} \\ 0 & \underbrace{u_{2,2}} & \underbrace{u_{2,3}} \\ 0 & u_{3,2} & \underbrace{u_{3,3}} \end{pmatrix}, \tag{7}$$

where we have indicated by an underbrace terms that will vanish for vanishing wall deformation $\boldsymbol{\xi} \to 0$. Note that for the rigid-wall case $\boldsymbol{\xi} \equiv 0$, we have $u_{2,2} = 0$ from continuity, and $u_{i,3} = 0$ because the velocity vanishes identically at the wall. We now proceed to eliminate all those terms in (4) that are quadratic in quantities that vanish when $\boldsymbol{\xi} = 0$. The precise magnitude of the errors that this step incurs will be discussed below. The boundary conditions with the quadratic terms eliminated will be referred to as the "ultra-linearized" boundary conditions,

$$\begin{aligned} u_1 \quad + \quad U_{1,2}\xi_2 \quad + \quad u_{1,2}\xi_2 \quad &= \quad \dot{\xi}_1, \\ u_2 \quad &= \quad \dot{\xi}_2, \\ u_3 \quad + \quad u_{3,2}\xi_2 \quad &= \quad \dot{\xi}_3. \end{aligned} \tag{8}$$

Note that the above set of boundary conditions still contains two terms, $u_{1,2}\xi_2$ and $u_{3,2}\xi_2$, that are nonlinear in the dependent variables of our problem. Because of the complications associated with this nonlinearity, we want to drop these terms, too. We can estimate their magnitude from experimental data in Townsend [7]. There we find that at $y^+ = 5$, where $y^+ = u_\tau y/\nu$, $u_1/u_\tau = 1.54$, while $u_3/u_\tau = 0.306$. The behavior of both is linear between $y^+ = 5$ and the wall. We may thus estimate

$$\begin{aligned} u_{1,2} \quad &\approx \quad 0.308\frac{u_\tau^2}{\nu} \\ u_{3,2} \quad &\approx \quad 0.0612\frac{u_\tau^2}{\nu} \end{aligned} \tag{9}$$

for values of y^+ between 0 and 5. Since we have $U_{1,2} \approx u_\tau^2/\nu$, we see that these derivatives (at least, $u_{1,2}$) are not substantially smaller than the mean velocity derivative. However, if we accept an accuracy of 30%, we can write

$$\begin{aligned} u_1 \quad + \quad U_{1,2}\xi_2 \quad &= \quad \dot{\xi}_1 \\ u_2 \quad &= \quad \dot{\xi}_2 \\ u_3 \quad &= \quad \dot{\xi}_3. \end{aligned} \tag{10}$$

We can now estimate the orders of magnitude of the three components,

$$u_1 \approx \frac{u_\tau^2}{\nu}\xi_1, \quad u_2 \approx \frac{u_\tau^2}{\nu}\xi_2, \quad u_3 \approx \frac{u_\tau^2}{\nu}\xi_3, \tag{11}$$

and we can also accurately estimate the magnitude of the omitted components (the ones that were quadratic in terms which vanish when ξ vanishes). A single example will be sufficient:

$$\frac{u_{1,3}\xi_3}{u_1} \approx \xi_3 k_3, \tag{12}$$

and the others are similar. k_3 is the wavenumber in the z-direction. Thus, these terms will be small if the displacement of the surface is small relative to the wavelength of the surface disturbance. This will almost always be the case. Finally, let us consider the terms that do not vanish when ξ vanishes. We obtain

$$\frac{u_{1,2}\xi_2}{u_1} \approx 0.308\frac{\xi_2}{\xi_1}, \quad \frac{u_{3,2}\xi_2}{u_3} \approx 0.0612\frac{\xi_2}{\xi_3}. \tag{13}$$

We have thus shown that by neglecting $u_{1,2}\xi_2$ relative to $U_{1,2}\xi_2$, we make a maximum error of about 30%. Henceforth, for the low-dimensional model, we will assume (10), because of its linearity. The relatively large potential error that is involved in this assumption is one of the reasons why this project will also include direct numerical simulations of the turbulent flow over a compliant boundary, in order to be able to assess the effect of the various simplifications involved in the modeling process. Of course, for the direct numerical simulations that we are planning, the above two terms will be kept. Since we are using a dynamical coordinate transformation technique for this simulation (see below), there is no difficulty in treating the boundary conditions exactly, so the above approximations are not necessary in that case.

3.2.3 The Pressure Term

In the dynamical systems model for the flow as given by (2) above, the pressure term in the Navier-Stokes equations has been neglected. Formally, after Galerkin projection, the pressure term results in an expression of the form

$$\left(\boldsymbol{\psi}^{(j,k)}, \mathbf{grad}\,(p)\right) = \int \boldsymbol{\psi}^{j,k*} \cdot \mathbf{grad}\,(p)\, d\boldsymbol{x}, \tag{14}$$

where $\boldsymbol{\psi}^{(j,k)}$ is one of the three-dimensional, vector-valued basis functions being used in the projection (in our case, $\boldsymbol{\psi}^{(j,k)}(y,z) = \boldsymbol{\varphi}^{(j,k)}(y)\mathrm{e}^{\mathrm{i}kz}$), and the integral is over the flow domain of interest. Using the integral theorems and the fact that the $\boldsymbol{\psi}^{(j,k)}(y,z)$ are solenoidal, this can be written as a surface integral

$$\left(\boldsymbol{\psi}^{(j,k)}, \mathbf{grad}\,(p)\right) = \oint \boldsymbol{\psi}^{(j,k)*} \cdot \boldsymbol{n}\, p\, dS, \tag{15}$$

where $\boldsymbol{n}$ is the outward normal on the boundary S of the domain. Using a Fourier representation of the pressure, $p(y,z) = \sum_k \hat{p}(k,y)\mathrm{e}^{\mathrm{i}kz}$, we find that the only remaining terms are

$$\left(\boldsymbol{\psi}^{(j,k)}, \mathbf{grad}\,(p)\right) = -\hat{p}(k,0)\varphi_2^{j,k*}(0) + \hat{p}(k,y_m)\varphi_2^{j,k*}(y_m), \tag{16}$$

where y_m is the height of our domain.

In [1, 5] it is shown that the term from the upper boundary mainly acts as a random disturbance to keep the solution at a finite average distance in phase space from the attracting heteroclinic orbit, which is responsible for the bursting events in the near-wall turbulent flow. It is demonstrated there that this pressure term, however, does not fundamentally alter the dynamics of the system. In addition, since we are interested only in comparing the behavior of the compliant-wall system to the one with the fixed wall, omission of the last term in (16) is justified. However, the first term on the right-hand side of (16) is zero only for the fixed wall, but will in general be non-zero for a moving wall. We therefore want to add this term to our dynamical equations, so that we end up with

$$\begin{aligned}\dot{a}^{(j,k)} &= \sum_n \left(b_{nk}^{j,\text{meanvel}} + (1+2\pi\alpha) b_{nk}^{j,\text{visc}} \right) a^{(n,k)} \\ &+ \sum_{k',p,q} c^j_{(k',k-k')_{pq}} a^{(p,k')} a^{(q,k-k')} \\ &+ \sum_{n,k',p,q} d^j_{nk'pq} a^{(n,k)} \Re \left(a^{(p,k')} a^{(q,k')*} \right) + \frac{1}{\rho} \hat{p}(k,0) \varphi_2^{j,k*}(0). \end{aligned} \tag{17}$$

3.2.4 Equations for the Dynamics of the Wall

We model the compliant surface in the Fourier space spanned by the spanwise wavenumbers k as a linear damped mass-spring system driven by the fluid stress at the wall. The stiffness and damping parameters may be different for different spanwise wavenumbers k. In the streamwise and spanwise directions, the deformations of the wall are driven by the shear stress which is easily accessible in the models as a linear term in the model coefficients.

$$M_1^k \ddot{\hat{\xi}}_1^k + D_1^k \dot{\hat{\xi}}_1^k + K_1^k \hat{\xi}_1^k = \hat{\tau}_1^k|_{wall} = \sum_n a^{(j,k)} \varphi_{1,2}^{(j,k)} \tag{18}$$

$$M_3^k \ddot{\hat{\xi}}_3^k + D_3^k \dot{\hat{\xi}}_3^k + K_3^k \hat{\xi}_3^k = \hat{\tau}_3^k|_{wall} = \sum_n a^{(j,k)} \varphi_{3,2}^{(j,k)} \tag{19}$$

The wall-normal deformations of the compliant surface are driven by the pressure fluctuations at the boundary.

$$M_2^k \ddot{\hat{\xi}}_2^k + D_2^k \dot{\hat{\xi}}_2^k + K_1^k \hat{\xi}_2^k = \hat{p}(0,k) \tag{20}$$

We employ capital letters to describe the properties of the compliant surface for clarity; the lower indices allow for the elastic properties of the wall to be different for different coordinates.

3.2.5 Basis Functions

We choose to base our low-dimensional model for the turbulent boundary layer over a compliant surface on the eigenfunctions of the rigid-wall boundary layer. Since these eigenfunctions

have $\varphi_i^{(1,k)} = 0$ at the wall and thus do not allow us to satisfy the boundary conditions (10). we need to introduce additional eigenfunctions to account for the motion of the compliant surface. In the absence of surface compliance, our models will revert to the rigid-wall case. Lacking an experimental or computational database on the turbulent flow over a compliant surface, we are reverting to derive our additional eigenfunctions in an *ad hoc* fashion. We choose additional eigenfunctions as solutions of the Stokes equation with periodic motion of the wall.

We will first approach the Stokes problem with boundary conditions corresponding to the oscillation of the wall in the streamwise direction. Since our low-dimensional model for the rigid-wall boundary layer is built upon a Fourier decomposition of the velocity field, we will use the Stokes equation to generate an eigenfunction for each wavenumber k,

$$\left(\Delta - \frac{1}{\nu}\frac{\partial}{\partial t}\right) u = 0,$$

$$\Rightarrow \left[\frac{\partial^2}{\partial y^2} - \left(k^2 + \frac{1}{\nu}\frac{\partial}{\partial t}\right)\right] \hat{u}(k,y,t) = 0, \tag{21}$$

and we will then proceed to assign these solutions to our basis functions $\varphi_1^{2,k}$. The velocity field is subject to the boundary conditions

$$\hat{u}(k,0,z) = cos(\beta t), \tag{22}$$

$$\hat{u}(k, y \to \infty, t) \to 0. \tag{23}$$

In order to satisfy the oscillating boundary conditions, the velocity field $u(y,t)$ can be represented as a superposition of left- and right-running traveling waves,

$$\hat{u}(k,y,t) = \hat{u}^+(k,y)\mathrm{e}^{\mathrm{i}\beta t} + \hat{u}^-(k,y)\mathrm{e}^{-\mathrm{i}\beta t}. \tag{24}$$

We may solve separately for $\hat{u}^-(k,y)$ and $\hat{u}^+(k,y)$ from the governing equation and boundary conditions.

$$\hat{u}^+(k,y) = A^+\mathrm{e}^{y\sqrt{k^2+\mathrm{i}\beta}} + B^+\mathrm{e}^{-y\sqrt{k^2+\mathrm{i}\beta}}, \tag{25}$$

$$\hat{u}^-(k,y) = A^-\mathrm{e}^{y\sqrt{k^2-\mathrm{i}\beta}} + B^-\mathrm{e}^{-y\sqrt{k^2-\mathrm{i}\beta}}. \tag{26}$$

In order for $\hat{u}(y,t)$ to decay at infinity, the first term in both u^+ and u^- must disappear, so that $A^+ = A^- = 0$. The boundary condition at the wall may be satisfied by u^+ and u^- together,

$$\hat{u}(k,y=0,t) = u^+(k,y=0,t)\mathrm{e}^{\mathrm{i}\beta t} + u^-(k,y=0,t)\mathrm{e}^{-\mathrm{i}\beta t} \tag{27}$$

$$= B^+\mathrm{e}^{\mathrm{i}\beta t} + B^-\mathrm{e}^{-\mathrm{i}\beta t} \tag{28}$$

$$= \cos(\beta t) \tag{29}$$

The choice $B^+ = B^- = \frac{1}{2}$ satisfies the boundary conditions and results in the following form for $u(y,t)$:

$$\hat{u}(k,y,t) = \frac{1}{2}e^{i\beta t}e^{-y\sqrt{k^2+i\beta}} + \frac{1}{2}e^{-i\beta t}e^{-y\sqrt{k^2-i\beta}} \tag{30}$$

$$\tag{31}$$

We choose the eigenfunction which represents streamwise compliance from the initial value of $\hat{u}(k,y,t)$, i.e. $\varphi_1^{(2,k)}(y) = \hat{u}(k,y,t=0)$, $\varphi_2^{(2,k)}(y) = \varphi_3^{(2,k)}(y) = 0$. This choice for the form of the eigenfunction will permit the boundary conditions on the streamwise component of velocity to be satisfied.

We would ideally prefer each additional eigenfunction to have only a single component with a non-zero boundary condition. This will not always be possible when we account for the motion of the wall in all three directions, and the eigenfunctions are orthogonalized. But in the current case of strictly wall-normal motions and using the "ultra-linearized" boundary conditions (10), the additional eigenfunctions may be formulated in this fashion with $\varphi_1^{(2,k)}(y=0) \neq 0$ and $\varphi_2^{(3,k)}(y=0) \neq 0$. All other components are zero at the wall. In fact, the wall-normal and spanwise components of $\varphi_k^{(2)}$ and the streamwise component of $\varphi_k^{(3)}$ are strictly zero.

We now determine the additional eigenfunctions for the wall-normal motion of the wall in a similar fashion, using the streamfunction formulation of the Stokes equation:

$$\left(\frac{\partial^2}{\partial y^2} - k^2\right)\left[\frac{\partial^2}{\partial y^2} - \left(k^2 + \frac{1}{\nu}\frac{\partial}{\partial t}\right)\right]\Psi(k,y,t) = 0 \tag{32}$$

As before, we superpose left- and right-running wave solutions to this equation $\Psi(k,y,t) = e^{i\beta t}\Psi^+(k,y) + e^{-i\beta t}\Psi^-(k,y)$, and we apply the boundary conditions at infinity to Ψ^+ and Ψ^- to eliminate the terms which grow exponentially. Next, we enforce the boundary condition on the spanwise velocity $\partial\Psi(y=0,k)/\partial y = 0$. The two wave solutions are combined to satisfy the time-varying boundary conditions at the wall, $ik\Psi(y=0,k) = \cos(\beta t)$. This procedure allows the formation of a divergence-free additional eigenfunction which in turn allows the low-dimensional models to satisfy the boundary conditions at the compliant surface. The resulting basis functions are shown in Fig. 1.

After the additional eigenfunctions are obtained as solutions of Stokes problems, the complete set of basis functions is orthogonalized using a Gram-Schmidt procedure. This gives

$$\begin{aligned}
\varphi_1^{(2,k)} &\rightarrow \varphi_1^{(2,k)} - \varphi_1^{(1,k)}\frac{\left(\varphi_1^{(2,k)}, \varphi_1^{(1,k)}\right)}{\left(\varphi_1^{(1,k)}, \varphi_1^{(1,k)}\right)}, \\
\varphi_2^{(2,k)} &\rightarrow 0, \\
\varphi_3^{(2,k)} &\rightarrow 0,
\end{aligned} \tag{33}$$

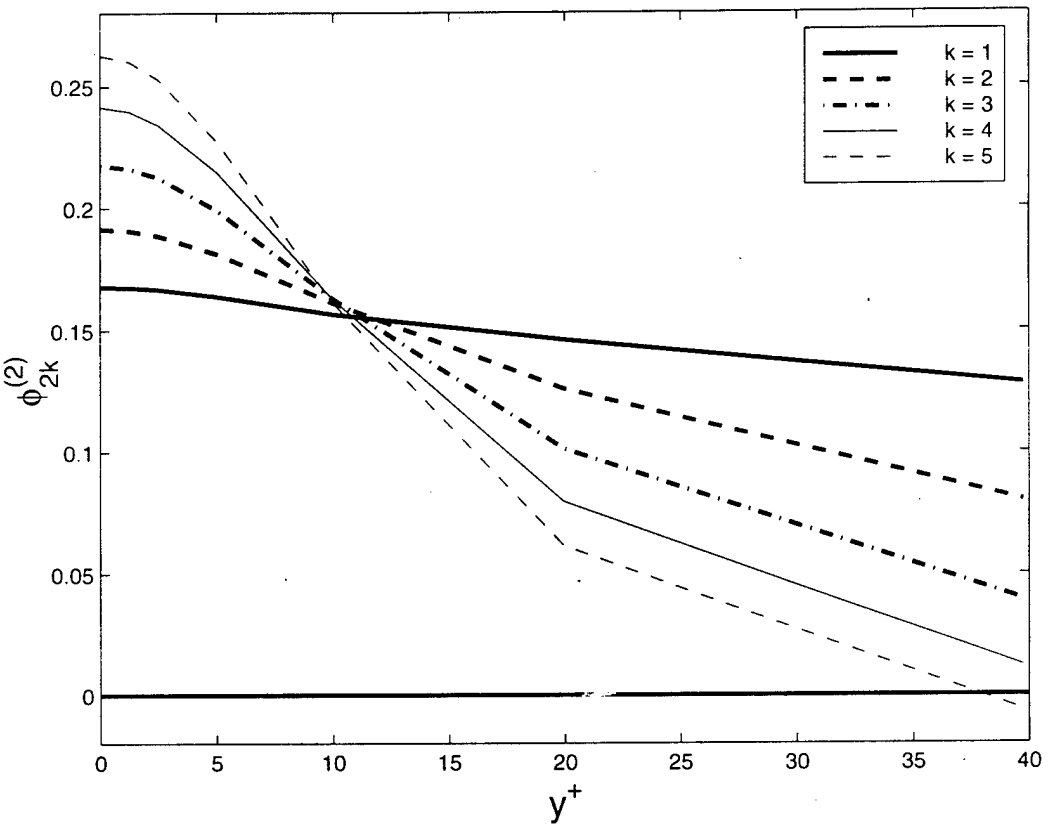

Figure 1: The wall-normal component of the compliant-wall eigenfunctions obtained from the Stokes equations, denoted $\varphi^{(2)}_{2_k}(y)$.

and

$$\begin{aligned}
\varphi_1^{(3,k)} &\rightarrow 0, \\
\varphi_2^{(3,k)} &\rightarrow \varphi_2^{(3,k)} - \varphi_2^{(1,k)} \frac{\left(\varphi_2^{(3,k)}, \varphi_2^{(1,k)}\right) + \left(\varphi_3^{(3,k)}, \varphi_3^{(1,k)}\right)}{\left(\varphi_2^{(3,k)}, \varphi_2^{(3,k)}\right) + \left(\varphi_3^{(3,k)}, \varphi_3^{(3,k)}\right)}, \\
\varphi_3^{(3,k)} &\rightarrow \varphi_3^{(3,k)} - \varphi_3^{(1,k)} \frac{\left(\varphi_2^{(3,k)}, \varphi_2^{(1,k)}\right) + \left(\varphi_3^{(3,k)}, \varphi_3^{(1,k)}\right)}{\left(\varphi_2^{(3,k)}, \varphi_2^{(3,k)}\right) + \left(\varphi_3^{(3,k)}, \varphi_3^{(3,k)}\right)}.
\end{aligned} \tag{34}$$

The new basis functions are finally normalized so that $(\varphi^{i,k}, \varphi^{i,k}) = 1$.

3.2.6 Six-Mode Model with Wall-Normal Compliance

The relations (10), (17), and (18–20) constitute a complete set of evolution equations for the coefficients of the eigenfunctions as well as evolution equations for the motion of the wall. In the following, we will further simplify this model by assuming that the only significant motion of the wall is in the wall-normal direction, which means that we will drop (18) and (19). In this case we need only two additional basis functions (the Stokes modes given above) to satisfy the wall-normal and streamwise boundary conditions. This way we end up with a model that includes one POD mode from the fixed-wall case, one Stokes mode for the wall-normal and streamwise coordinate boundary conditions, respectively, and one mode for the motion of the wall, which is later eliminated by using the coupling between wall and fluid motion. Each of the three wall-normal modes is then multiplied by one of two Fourier modes, which brings the total to six complex modes that make up this model.

We choose to determine the coefficients for the additional eigenfunctions from the boundary conditions at the wall. The pressure may then be determined from the evolution equation for the additional eigenfunction representing the wall-normal motion of the wall $\varphi_k^{(3)}$.

$$\begin{aligned}
\hat{p}(k, y=0) \approx \frac{\rho}{\varphi_2^{(3,k)*}(y=0)} \quad & \left[\dot{a}^{(3,k)} - \sum_p b_{kp}^{(3)} a^{(p,k)} \right. \\
& \left. - \sum_{k',p,q} c_{(k',k-k')_{pq}}^{(3)} a^{(p,k')} a^{(q,k-k')} \right].
\end{aligned} \tag{35}$$

The cubic terms disappear because this additional eigenfunction is defined to have no streamwise component, and there is no streamwise variation in our model. When this expression is substituted into the equation for the wall-normal motion of the wall (20), the time derivative term merges into the $\ddot{\xi}_2^k$-term resulting in a new effective mass of the wall $\tilde{M}_2^k$. In fact, $\dot{\xi}_2^k = a^{(3,k)} \varphi_2^{(3,k)}$ since $\boldsymbol{\varphi}^{(3,k)}$ is the only eigenfunction with a non-zero vertical velocity at the

wall. Normalizing with this new mass using

$$\tilde{M} = M + \rho/(\phi_{2_k}^{(3)}\phi_{2_k}^{(3)^*})|_w, \tag{36}$$

$$\tilde{\rho} = \rho/(\tilde{M}\phi_{2_k}^{(3)^*}|_w), \tag{37}$$

$$\tilde{D} = D/\tilde{M}, \tag{38}$$

$$\tilde{K} = K/\tilde{M}, \tag{39}$$

results in the following low-dimensional model for the flow over a compliant surface:

$$\dot{a}^{(1,k)} = \sum_p b_{pk}^{(1)} a^{(p,k)} + \sum_{k',p,q} c_{(k',k-k')_{pq}}^{(1)} a^{(p,k')} a^{(q,k-k')} + \sum_{r,k',p,q} d_{rk'pq}^{(1)} a^{(r,k)} \Re\left(a^{(p,k')} a^{(q,k')*}\right), \tag{40}$$

$$\ddot{\hat{\xi}}_2^k + \tilde{D}_2^k \dot{\hat{\xi}}_2^k + \tilde{K}_2^k \hat{\xi}_{2_k} \approx \tilde{\rho}\left[\sum_p b_{kp}^{(3)} a^{(p,k)} + \sum_{k',p,q} c_{(k',k-k')_{pq}}^{(3)} a^{(p,k')} a^{(q,k-k')}\right], \tag{41}$$

$$a^{(2,k)} = \frac{\hat{\xi}_2^k \frac{\partial U}{\partial y}|_{y=0}}{\varphi_1^{(2,k)}|_{y=0}}, \tag{42}$$

$$a^{(3,k)} = \frac{\dot{\hat{\xi}}_2^k}{\varphi_2^{(3,k)}|_{y=0}}. \tag{43}$$

3.3 Results

In the following, we will report the findings we obtained from an investigation of the above six-mode model, where we have used two spanwise Fourier modes k for each of the basis functions. As a result, we are looking at the behavior of a model described by a system of ODEs of order 12.

We started our investigation of this model by systematically varying $\tilde{\rho}$, $\tilde{D}$ and $\tilde{K}$ as our input parameters, and monitoring the resulting bursting frequency as our output parameter. The role of $\tilde{\rho}$ is to determine the relative strength of the wall forcing. Increasing $\tilde{\rho}$ increases the amplitude of the wall motion, and *vice versa*. We tried values of $\tilde{\rho}$ between $\tilde{\rho} = 0.01$ and $\tilde{\rho} = 1$, within which range our findings do not change qualitatively. For values of $\tilde{\rho}$ significantly smaller than that, the wall motion is too small to have a noticeable effect, and for values of $\tilde{\rho}$ larger than that range, the dynamics of our system changes qualitatively, so that the appropriateness of the model becomes questionable.

We found that the damping constant $\tilde{D}$ has relatively little effect (the reason for this will become clear below), whereas the stiffness $\tilde{K}$ turned out to be the most important parameter. Varying this stiffness parameter we found that the bursting frequency could be reduced by as much as 30%. We note that one would expect this to correspond to a drag reduction of the same order, although there is a possibility that the intensity of the bursts changes through the influence of the compliant wall, which could modify the actual value of drag reduction that is realized. While we do not see a change in the quality of the bursts in our model, this might be an artifact of the modeling process, which is another reason for us to check the findings from our model through a direct simulation that we are currently working on.

Fig. 2 shows a comparison of the phase-space portraits for the cases of a rigid and a compliant wall, respectively. The parameters we have chosen for the compliant wall are the ones that give minimum bursting frequency. The comparison of the two cases clearly shows that the qualitative dynamics of the flow is hardly changed at all by the presence of the compliant wall. This is important because it gives credence to our assumption that we can still describe the velocity distribution of the compliant-wall flow by using the most energetic eigenmode from a fixed-wall case.

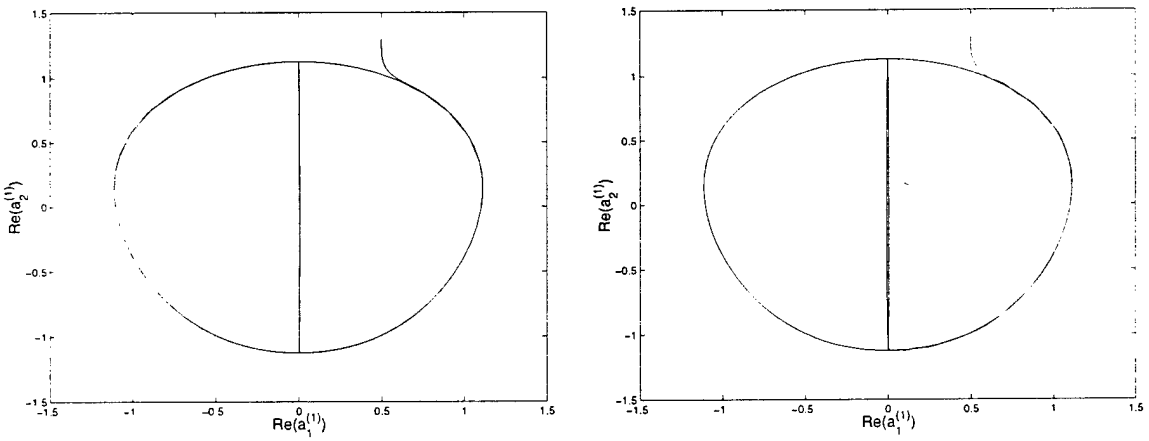

Figure 2: Phase-space projection onto the plane spanned by the real parts of the coefficients of the POD modes for the first and second Fourier mode, respectively. a), fixed wall, b), compliant wall. Parameters where $\tilde{d} = 0.1$, $\tilde{\rho} = 0.1$, $\tilde{k} = 500$.

Fig. 3 shows a comparison of the behavior in time of the coefficient of the most energetic POD mode. These time traces exemplify the intermittent nature of the flow dynamics: the flow stays calm for extended periods of time (the plateaus in Fig. 3), corresponding to the rolls being stationary, or very slowly drifting from side to side. Then, during a burst (the steep gradients in Fig. 3), the rolls begin to move violently, break down, and are recreated with a phase shift of a half wavelength.

Most significantly, however, the figure shows that for the compliant-wall case, the quiescent periods are longer, which corresponds to a reduced bursting frequency. Quantitatively, it turns out that in this case the bursting frequency has been reduced by about 30%. We should alert the reader to the fact that the increase in inter-burst time for the compliant-wall case is a transient effect for the numerical simulations shown in the figures. As discussed in [1] (see also [5] for a more detailed discussion), for a model without external disturbances, the inter-burst times should become longer and longer as the system gets closer to the heteroclinic cycle. However, due to finite truncation errors, any numerical simulation will show a convergence of the inter-burst times towards a finite value. The ultimate value that one finds in a numerical solution is a function of the numerical accuracy of the integration scheme that was used and has no physical meaning. In a real flow, on the other hand, there will be pressure disturbances acting on the upper boundary of the near-wall region we are considering here. In that case, inter-burst times depend on the magnitude of these pressure disturbances as well as on how strongly attracting the heteroclinic cycle is. If we have a heteroclinic cycle that is more strongly attracting, then, on average, the solution will be closer to the heteroclinic cycle, which results in longer inter-burst times. This is precisely the scenario that is indicated by the longer inter-burst times we observed during the transients in our numerical experiments. The prolonged inter-burst periods in the transients demonstrate that the heteroclinic cycle for the compliant wall model is more attracting, and hence, if numerical accuracy were not a factor, inter-burst times would consistently be higher for the compliant-wall case.

Finally, we should note that within our numerical accuracy the location of the heteroclinic cycles is identical for the rigid-wall and the compliant-wall case. For Fig. 3 we have started from identical initial conditions for both the fixed-wall and the compliant-wall case, which means that the results shown in that figure do indeed demonstrate that the heteroclinic cycle for the compliant-wall case is more strongly attracting than the one for the fixed wall. In further numerical experiments with different initial conditions (not shown here) we found qualitatively the same behavior.

Our last figure shows a representation of the temporal dynamics of the wall motion itself. We can see that the frequency of the wall motion is about a factor of 50 higher than the bursting frequency. In addition, the reader should take note of the extremely small amplitude of the wall fluctuations as shown in Fig. 4. This observation validates our assumption of small wall deformation we made in deriving our model, and it also demonstrates why the value of the damping constant in our model has little influence on the dynamics of the flow. At these tiny fluctuation levels, the energy that is dissipated in the compliant wall is many orders of magnitude lower that the energy dissipation of the flow, so one would expect to see next to no influence of energy dissipation in the wall on the flow dynamics.

3.3.1 Direct Numerical Simulation

The problem we are considering is basically a fluid-solid problem. On the fluid side, we have the incompressible NS equation as the model for fluid motion. On the solid side, we

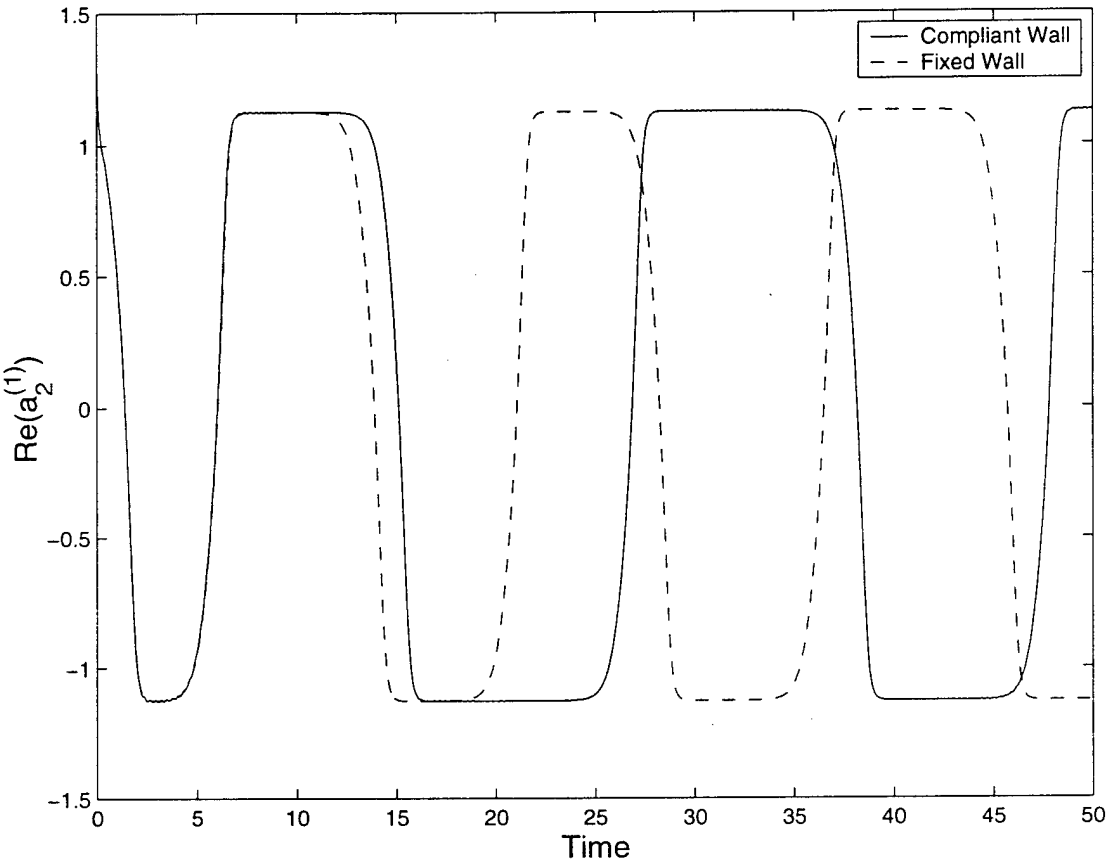

Figure 3: Comparison of the time behavior of the real part of the coefficient of the POD mode for the second Fourier mode. Solid, compliant wall, dashed, fixed wall. Same parameters for the compliant wall as above.

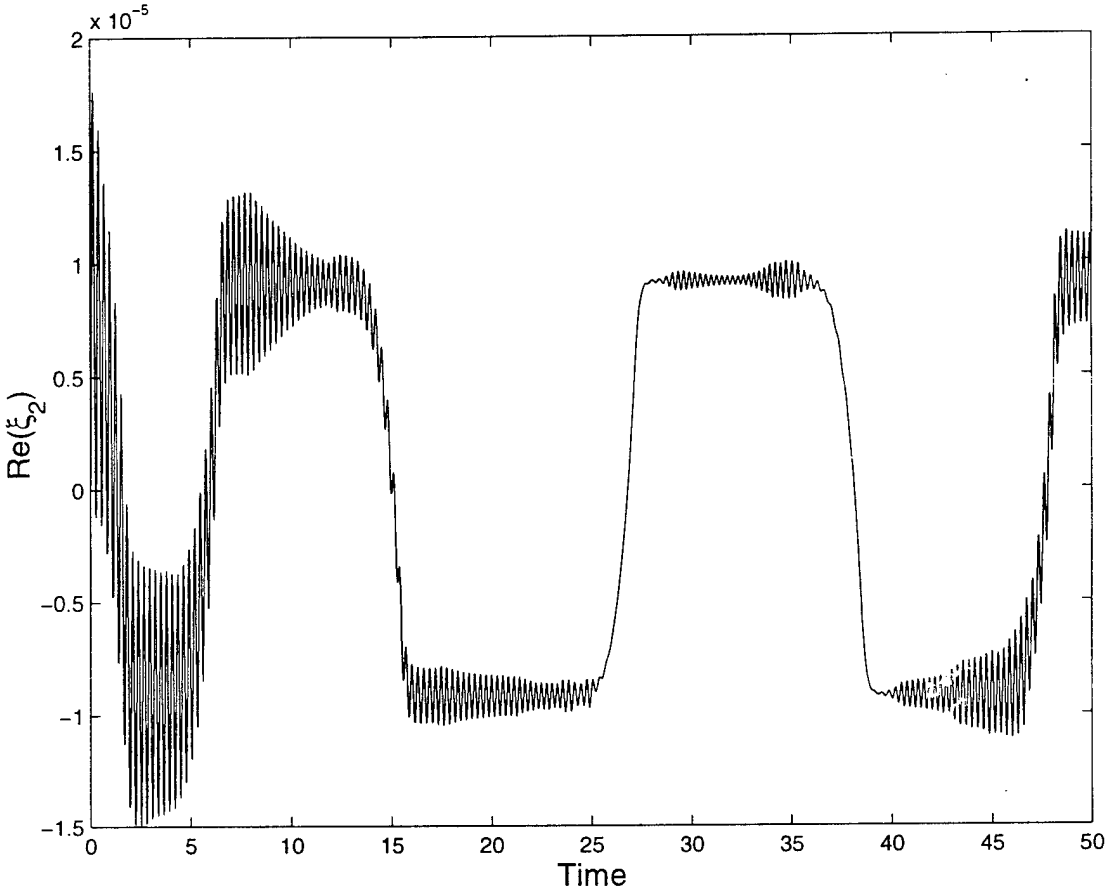

Figure 4: Dynamics of the wall motion (second Fourier mode). Same parameters for the compliant wall as above.

use a spring-supported elastic plate to model the compliant wall. The equation governing the wall-normal motion nondimensionalized by the average half channel height h and the laminar centerline velocity u_0 reads

$$C_0\frac{\partial^2\eta}{\partial t^2}+C_1\frac{\partial\eta}{\partial t}+C_2\left(\frac{\partial^4\eta}{\partial x_1^4}+\frac{\partial^4\eta}{\partial x_3^4}+2\frac{\partial^4\eta}{\partial x_1^2x_3^2}\right)+C_3\eta-C_x\frac{\partial^2\eta}{\partial x_1^2}-C_z\frac{\partial^2\eta}{\partial x_3^2}=-p_w, \tag{44}$$

where η is the wall-normal displacement, p_w is the pressure disturbance on the wall and C_0, C_1, C_2, C_3, and $C_x(C_z)$ are the nondimensional wall properties defined as

$$\begin{aligned} C_0&=\frac{\rho_m b}{\rho h}, \quad C_1=\frac{1}{Re}\frac{dh}{\rho\nu}, \quad C_2=\frac{1}{Re^2}\frac{B}{\rho h\nu^2},\\ C_3&=\frac{1}{Re^2}\frac{K_E h^3}{\rho\nu^2}, \quad C_x=\frac{1}{Re^2}\frac{T_x h}{\rho\nu^2}, \quad C_z=\frac{1}{Re^2}\frac{T_z h}{\rho\nu^2}, \end{aligned} \tag{45}$$

The wall parameters are: the plate density ρ_m and thickness b, the wall damping coefficient d, the flexural rigidity of the plate B, the streamwise (spanwise) tension per unit width $T_x(T_z)$ and the spring stiffness K_E; ρ is the density of the fluid and ν is its kinematic viscosity. The turbulent channel flow we simulate is assumed periodic in the streamwise(x_1 or x) and spanwise(x_3 or z) directions and has a rigid upper and a compliant lower wall that are separated by an average distance of $2h$ in the wall-normal(x_2 or y) direction. Re is its Reynolds number based on h and u_0.

The main difficulty of the simulation is to handle the boundary conditions at the moving compliant wall. We use a time-varying coordinate transformation to eliminate the deformation of the compliant boundary in the computational domain. The continuity equation in the computational coordinate system becomes

$$u^i_{;i} \;=\; 0, \tag{46}$$

and the momentum equation in the rotational form becomes

$$\frac{\partial u^i}{\partial t}=-\frac{\partial T^{-1}}{\partial t}\frac{\partial u^i}{\partial x_2}+u^j g^{ik}(u_{j;k}-u_{k;j})-g^{ij}\frac{\partial p}{\partial x_j}+\frac{1}{Re}(g^{jk}u^i_{;k})_{;j}, \tag{47}$$

where u^i is a contravariant velocity component, the semicolon denotes covariant differentiation, T^{-1} is the inverse coordinate transformation function in the wall-normal direction, and g^{ij} is the contravariant metric tensor of the transformation. The equation for pressure p is obtained by taking a covariant differentiation with respect to x_i on the momentum equation and can be written as

$$\left(g^{ij}\frac{\partial p}{\partial x_j}\right)_{;i}=\left[-\frac{\partial T^{-1}}{\partial t}\frac{\partial u^i}{\partial x_2}+u^j g^{ik}(u_{j;k}-u_{k;j})\right]_{;i}. \tag{48}$$

The boundary conditions for velocity must also be transformed into the new coordinate system. The boundary conditions for pressure can then be determined indirectly from the incompressibility condition via an influence matrix technique. A Fourier-Galerkin and Chebyshev-Tau pseudospectral method for spatial discretization and a three-sub-step RK method for time advancement are used for solving the equations.

Results The computational domain sizes in the streamwise and spanwise directions are chosen to be π and $\frac{\pi}{3}$, respectively. The computation is carried out using $32 \times 65 \times 32$ (in x, y, z) grid points for a Reynolds number of 3300. In addition, as a reference case for comparisons we have simulated the turbulent flow in a canonical channel composed of two rigid walls with the same flow parameters as those for the compliant wall. For both cases the mean pressure gradient is calculated at each time step to enforce constant mass flux in the channel.

An important issue in the compliant-wall case is how to choose the compliant wall parameters. We currently choose them following [Semenov (1991)], while satisfying the numerical requirements of stability, the accuracy of the representation of the physical fluid-solid interaction, and an acceptable numerical time step. The damping factor of the compliant wall plays a key role in the simulations. It should be large enough to inhibit a dynamic instability of the interaction between the compliant wall and the turbulent flow. On the other hand, the compliant wall should move intensively enough so that it physically interacts with the turbulence rather than just generating some numerical noise in the computational system. These requirements lead to values for the wall parameters that are not very close to those of materials that others have used in their experiments, because the small pressure disturbance due to the low Reynolds number of our DNS cannot excite a sufficient motion of an experimental compliant wall. Nevertheless we believe to observe similar physics. The third numerical requirement is that the natural frequencies corresponding to pressure disturbances of high wave numbers have to be low enough to guarantee an acceptable time step in the numerical simulation. In a monoharmonic approximation for the compliant wall motion, the forcing pressure disturbance is given in the harmonic form

$$p_w = \mathrm{Re}[\hat{p}_w \mathrm{e}^{\mathrm{i}k_x x + \mathrm{i}k_z z - \mathrm{i}\sigma t}]. \tag{49}$$

The natural circular frequency of the free vibration f and the time constant of damping C for the compliant wall are then found to be

$$f = \begin{cases} 0 \quad \text{(no free vibration)} & \text{if } \beta \geq 2\omega, \\ \frac{1}{2}\left|\beta^2 - 4\omega^2\right|^{\frac{1}{2}} & \text{if } \beta < 2\omega, \end{cases} \tag{50}$$

$$C = \begin{cases} 2\left[\beta - (\beta^2 - 4\omega^2)^{\frac{1}{2}}\right]^{-1} & \text{if } \beta \geq 2\omega, \\ 2\beta^{-1} & \text{if } \beta < 2\omega, \end{cases} \tag{51}$$

where β and ω are defined as

$$\beta = \frac{C_1}{C_0}, \quad \omega^2 = \frac{1}{C_0}\left[C_2(k_x^4 + k_z^4 + 2k_x^2 k_z^2) + C_x k_x^2 + C_z k_z^2 + C_3\right]. \tag{52}$$

The steady amplitude (in wall units) of the compliant wall displacement r^+ and the normal velocity of the wall V_w^+ are

$$r^+ = \frac{K_d \hat{p}_w Re_\tau}{C_0 \omega}, \tag{53}$$

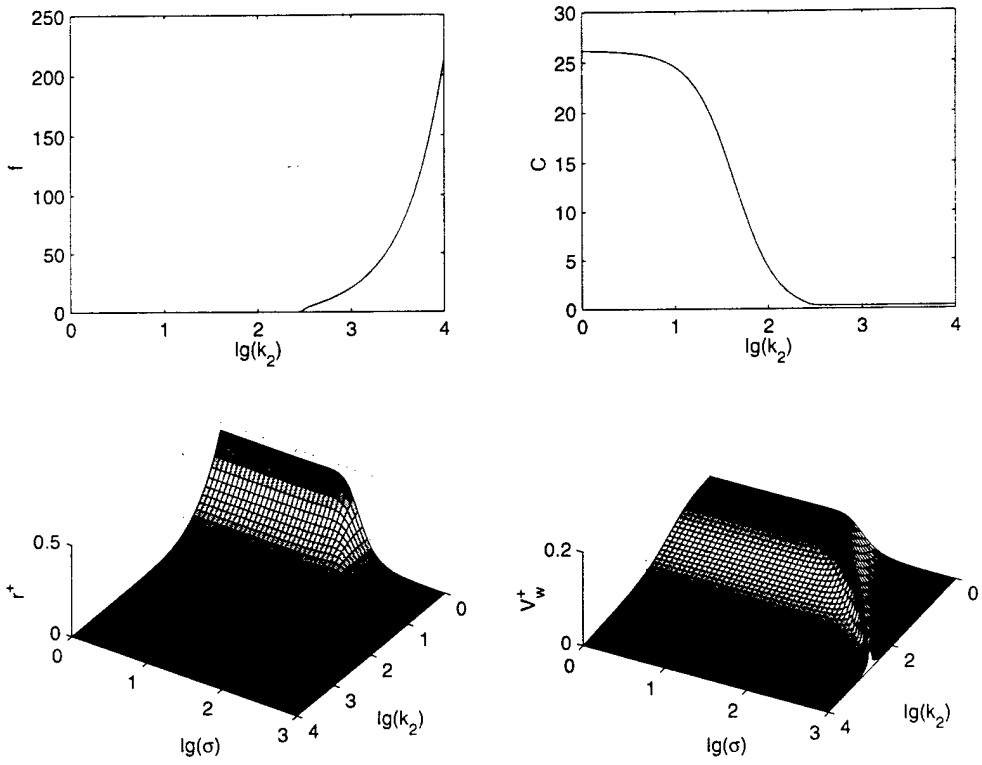

Figure 5: The results of the monoharmonic analysis for the compliant wall motion for $Re = 3300$, $Re_\tau = 140$, $\hat{p}_w = 0.01$, with $k_2 = k_x^2 + k_z^2$.

$$V_w^+ = \frac{K_d \hat{p}_w \sigma Re}{C_0 \omega Re_\tau}. \tag{54}$$

Here, Re_τ is the turbulent Reynolds number on the compliant wall, and K_d is the dynamic coefficient which can be calculated from

$$K_d = \left[\left(1 - \frac{\sigma^2}{\omega^2} \right)^2 + \frac{\beta^2 \sigma^2}{\omega^4} \right]^{-\frac{1}{2}}. \tag{55}$$

Figure 5 shows the results of a monoharmonic analysis for the compliant wall motion. These and the later simulation results indicate that the compliant wall we used in the simulation satisfies the numerical requirements. The flow and the compliant wall parameters in the simulation are given in Table 1.

Figure 6 shows the history of the total drag (represented by the mean streamwise pressure gradient) and the skin friction coefficients for the two cases. The skin friction on the compliant wall is 12% less than that on a rigid wall in the reference case, while they are about the same on all rigid walls in both cases.The turbulent Reynolds number is 138 based

ρ	$1000\,\mathrm{kg\ m^{-3}}$	ρ_m	$800\,\mathrm{kg\ m^{-3}}$
h	$0.005\,\mathrm{m}$	b	$0.003\,\mathrm{m}$
ν	$1 \times 10^{-6}\,\mathrm{m^2\ s^{-1}}$	d	$2000\,\mathrm{kg\ m^{-2}\ s^{-1}}$
Re	3300	B	$3 \times 10^{-9}\,\mathrm{kg\ m^{-2}\ s^{-2}}$
		T_x	$0.001\,\mathrm{kg\ s^{-2}}$
		T_z	$0.0001\,\mathrm{kg\ s^{-2}}$
		K_E	$10000\,\mathrm{kg\ m^{-2}\ s^{-2}}$

Table 1: Values of the flow and the compliant wall parameters.

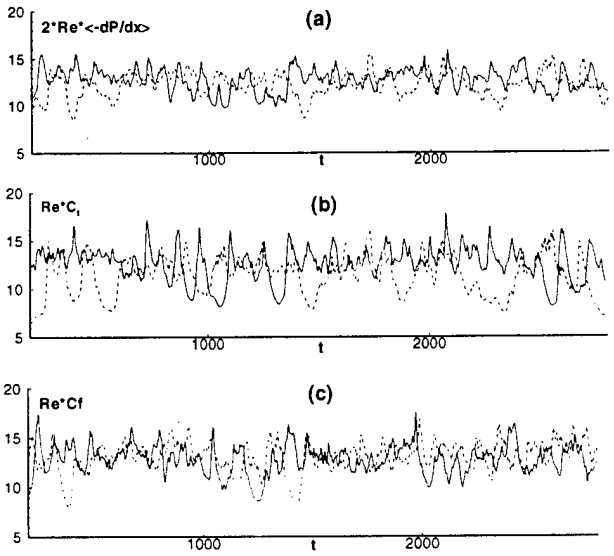

Figure 6: Time traces of (a) total drag, (b) skin friction on the compliant wall in the compliant wall case and a rigid wall in the reference case and (c) skin friction on the rigid wall in the compliant wall case and a rigid wall in the reference case. solid line: the reference case, dashed line: the compliant wall case.

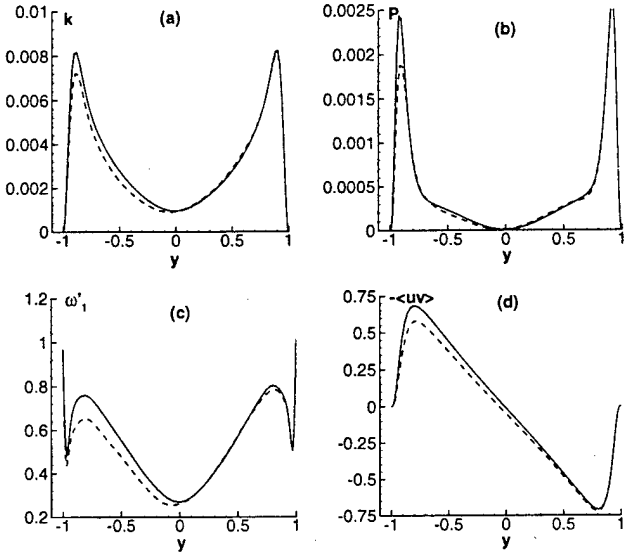

Figure 7: Comparisons of (a) turbulent kinetic energy, (b) turbulent kinetic energy production, (c) RMS streamwise vorticity and (d) Reynolds shear stress. The average position of the compliant wall is at $y = -1$. solid line: the reference case, dashed line: the compliant wall case

on the compliant wall friction velocity and 147 on a rigid wall. Consistent with these observations, we achieve a total drag reduction of 6% in a channel with one compliant wall. The amplitude of the compliant wall motion is so small that most of the present drag reduction is due to the wall-normal velocity of the compliant wall rather than the wall displacement and the total drag is almost completely from skin friction. It seems that the effects of the compliant wall on turbulence are localized, which can also be demonstrated by comparing the turbulence statistics in figure 7.

The magnitude of turbulent kinetic energy k, turbulent kinetic energy production P, RMS streamwise vorticity ω' and Reynolds shear stress $-\langle uv \rangle$ are reduced near the compliant wall as seen in figure 7. The quadrant analysis in figure 8 shows that the reduction of Reynolds shear stress is due to the decreased intensity of Q2 and Q4 events. As commonly observed in turbulent flows with skin friction reduction manipulations, the compliant wall shifts the log-law region in the mean streamwise velocity upwards, away from the wall (see figure 9). The mechanisms of skin friction reduction appear to be related to the stabilizing or weakening effects of the compliant wall on the near-wall streamwise vortices, which are regarded to play a dominant role in near-wall turbulent transport phenomena (Robinson 1991).

Instantaneous compliant wall shapes and the contours of wall-normal velocity at the wall at two instants are shown in figure 10. The skin friction on the wall is low at one instant and high at the other. The contours of streamwise fluctuating velocity in the x-z-planes

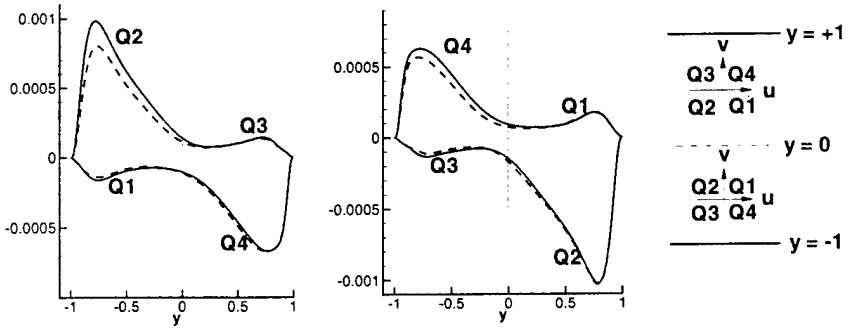

Figure 8: Comparisons of quadrant analysis. The average position of the compliant wall is at $y = -1$. solid line: the reference case, dashed line: the compliant wall case.

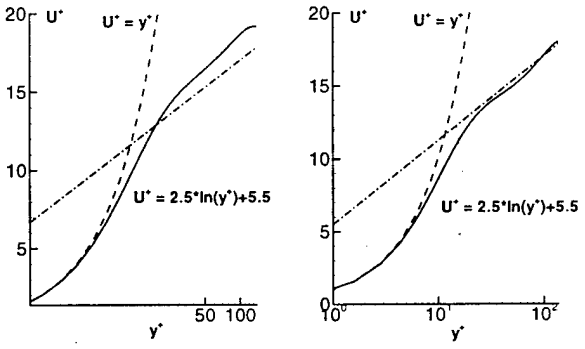

Figure 9: Mean streamwise velocity in the compliant wall case near (a) the compliant wall and (b) the rigid wall.

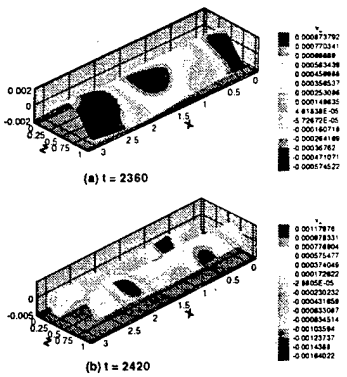

Figure 10: Wall-normal displacement and contours of wall-normal velocity at two instants of (a) low skin friction and (b) high skin friction on the compliant wall.

near the compliant wall are plotted at the same two instants in figure 11. From figure 10 and figure 11, it can be seen that the compliant wall forms a longitudinal ridge beneath a high-speed streak and a corresponding groove beneath a low-speed streak, even though the contours of the instantaneous wall-normal velocity at the wall are intermittent and oval-shaped. [Kang & Choi (2000)] made similar observations for the case of their active wall control for skin friction reduction. At the instant of low skin friction on the compliant wall, the near-wall streaky structures are very obvious. Their breakdown is observed at the instant of high skin friction at the wall.

Discussion First results of our direct numerical simulations of turbulence on a compliant wall indicate a clear potential for drag reduction. While it is true that the results described above were obtained for a somewhat non-generic case at a very low Reynolds number, we find that the effect of the compliant wall is limited to the near-wall region, which can be assumed to show a universal behavior that is only moderately affected by Reynolds number. It is therefore not unreasonable to assume that the behavior that we found for our low-Reynolds number case will persist into the range of higher Reynolds numbers, and for wide channels. Of course, this assumption will have to be tested in numerical simulations as well. We have already started such an investigation of turbulence in a wide compliant channel at the time of this report.

3.3.2 Conclusions

The low-dimensional model described above indicates that it might be possible to significantly reduce the drag of wall-bounded turbulent flow using a compliant wall of appropriate stiffness. The required stiffness for optimal reduction of bursting frequency has to be such that the eigenfrequency of the wall is one to two orders of magnitude higher than the bursting

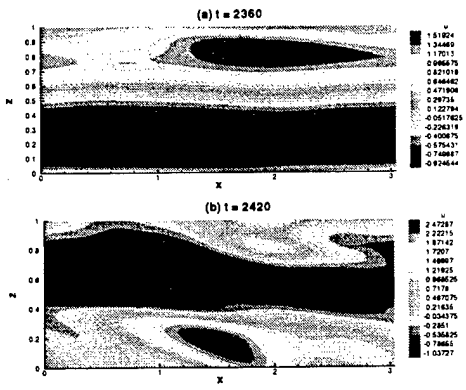

Figure 11: Contours of fluctuation streamwise velocity at the plane $y^+ = 2$ parallel to the average position of the compliant wall at two instants of (a) high skin friction and (b) low skin friction on the compliant wall.

frequency, which corresponds to a wall that will show only minute deformations under the action of the turbulent pressure fluctuations. This finding is compatible with the experimental results reported by Choi *et al.* [3].

Because of the smallness of the wall deformations it is clear that the internal damping of the wall material does not play a significant role in reducing turbulent fluctuations. Rather, the reduction in bursting frequency seems to be an indirect effect of the presence of the moving wall, which keeps the system close to its fixed point for a longer time.

We should also emphasize that we are well aware of the inherent danger of the simplifications we introduced in designing the model that is described above. It is for this reason that we are currently concentrating our efforts on developing a direct numerical simulation of turbulent flow over a compliant wall, which will be used to verify the predictions of our model as well as to refine the model as necessary. In particular, once we have the direct numerical simulation, we can use the data to directly calculate eigenfunctions for the compliant-wall case, so that we do not have to rely on the *ad hoc* Stokes eigenfunctions we were using in the present study. We expect this simulation to give us direct insight into the modifications of the flow dynamics that are caused by wall compliance, and thus to allow us to refine our modeling assumptions. As a final remark, we note that in this project we view direct numerical simulation and low-dimensional modeling as complementary techniques. Thus, our simulations will allow us to improve the model, and the improved model will give more accurate predictions of optimal parameters for drag reduction.

4 Personnel Supported

Faculty: John Lumley, Dietmar Rempfer
Graduate Students: Kiran Bhaganagar, Sheng Xu, Vejapong Juttijudata, Louise Parsons

5 Publications

5.1 Journal Articles:

- SAXENA, V.; LEIBOVICH, S.; BERKOOZ, G. (1999)
  Enhancement of the three-dimensional instability of free shear layers. *Journal of Fluid Mechanics.* **379**:23–38.

- REMPFER, D. (2000)
  On Low-Dimensional Galerkin Models for Fluid Flow. *Theoret. Comput. Fluid Dynamics* **14**:75–88.

5.2 Research reports (submitted, in review, in press):

- HAEUSSER, T.; LEIBOVICH, S. (1999)
  Pattern formation in the marginally unstable Ekman layer. *Journal of Fluid Mechanics.* In review.

- LEIBOVICH, S.; YANG, G. (1999)
  Turbulent flow in natural water bodies driven by wind and surface waves. *Journal of Fluid Mechanics.* In review.

- PODVIN, B.; LUMLEY, J. L.; BERKOOZ, G. (1999)
  Non-linear Kalman filtering for a turbulent channel flow. *AIAA Journal.* In review.

- REUTER, J.; REMPFER, D. (1999)
  High Order Vorticity-Velocity Method for the Simulation of Pipe Flow Transition. To appear in: *Appl. Num. Math.* **31**

- ALBUKREK, C.; URBAN, K.; DAHMEN, W.; REMPFER, D.; LUMLEY, J. (2000)
  Divergence-Free Wavelet Analysis of Turbulent Flows. Submitted to *Journal of Computational Physics.*

- XU, S.; REMPFER, D.; LUMLEY, J. (2001)
  Numerical Simulation of Turbulent Skin Friction Reduction by Wall Compliance. Submitted to *Journal of Fluid Mechanics.*

- REMPFER, D. (2001) On Boundary Conditions for Incompressible Navier-Stokes and Related Problems. Submitted to *Journal of Computational Physics.*

- BHAGANAGAR, K.; REMPFER, D.; LUMLEY, J. (2001)
  Direct Numerical Simulation of Spatial Transition to Turbulence using Fourth-Order Vertical Velocity Second-Order Vertical Vorticity Formulation. Submitted to *Journal of Computational Physics.*

5.3 Expository Articles, Books and Other Publications

- BLOSSEY, P. N. (1999)
  Drag reduction in near-wall turbulent flow. Ph. D. Thesis, Cornell University.

- BLOSSEY, P. N.; LUMLEY, J. L. (1999)
  Control of intermittency in near-wall turbulent flow. To appear in *Intermittency in Turbulent Flows and Other Dynamical Systems*, ed. C. Vassilicos, Cambridge University Press.

- LUMLEY, J. L. (1999)
  Engines: An Introduction. Cambridge, UK: Cambridge University Press.

- LUMLEY, J. L.; BLOSSEY, P. N. (1999)
  The low dimensional approach to turbulence. In *Modeling Complex Turbulent Flows*, ed. M. D. Salas, J. Hefner and L. Sakell, Kluwer Academic Press.

- LUMLEY, J. L.; BLOSSEY, P. N.; PODVIN-DELARUE, B. (1999)
  Low dimensional models, the minimal flow unit and control. To appear in *Fundamental Issues in Turbulence Research*, ed. A. Gyr, 1999.

- REMPFER, D. (1999)
  Dynamical Structures in Open Fluid Systems. In: *Evolution of Spontaneous Structures in Dissipative Continuous Systems.* (Eds. F. H. Busse, S. C. Müller), Springer.

- REMPFER, D. (1999)
  On Dynamical Systems obtained via Galerkin Projections onto Low-Dimensional Bases of Eigenfunctions. In *Fundamental Issues in Turbulence Research*, ed. A. Gyr, 1999.

6 Interactions

6.1 Conference Presentations

- P. N. Blossey and J. L. Lumley. Active control of near-wall turbulent flow. United Technologies Research Center, East Hartford, CT, January 1999. Invited.

- P. N. Blossey and J. L. Lumley. Active control of near-wall turbulent flow. Applied Mathematics Seminar, University of Wisconsin (Madison), February 1999. Invited.

- P. N. Blossey and J. L. Lumley. Active control of near-wall turbulent flow. Dynamic Systems and Controls Seminar, University of California, San Diego, March 1999. Invited.

- J. L. Lumley and P. N. Blossey. Control of intermittency in near-wall turbulent flow, Isaac Newton Mathematics Institute, Cambridge, UK, June 1999. Invited.

- D. Rempfer and J. L. Lumley. Low-Dimensional Models for Near-Wall Turbulent Flow: Applications for Active and Semi-Active Control. 6thh AIAA-CEAS Aeroacoustics Conference, Maui, HI, June 2000. Invited.
- D. Rempfer and J. L. Lumley. Low-Dimensional Models for Turbulent Shear-Flow Control. 20th International Congress of the International Union of Theoretical and Applied Mechanics, Chicago, IL, August/September 2000. Invited.
- C. Albukrek, D. Rempfer, J. Lumley, K. Urban, W. Dahmen. Divergence-Free Wavelet Analysis of Turbulent Flows. 53d Annual Meeting of The American Physical Society's Division of Fluid Dynamics, Washington, DC, November 2000. Contributed.
- D. Rempfer. The Fable of the Wall-Normal Pressure-Gradient Boundary Condition – Or: Why Muenchhausen was a Liar. 53d Annual Meeting of The American Physical Society's Division of Fluid Dynamics, Washington, DC, November 2000. Contributed.
- J. Gibson, D. Rempfer, J. Lumley. Boundary Conditions for Low-Dimensional Models of the Turbulent Boundary Layer. 53d Annual Meeting of The American Physical Society's Division of Fluid Dynamics, Washington, DC, November 2000. Contributed.
- K. Bhaganagar, D. Rempfer, J. Lumley. DNS of Spatial Transition to Turbulence in a Boundary Layer. 53d Annual Meeting of The American Physical Society's Division of Fluid Dynamics, Washington, DC, November 2000. Contributed.
- L. Parsons, D. Rempfer, J. Lumley. Low-Dimensional Model of the Interaction of Near-Wall Turbulence with a Compliant Boundary. 53d Annual Meeting of The American Physical Society's Division of Fluid Dynamics, Washington, DC, November 2000. Contributed.
- S. Xu, D. Rempfer, J. Lumley. Direct Numerical Simulation of the Interaction of Near-Wall Turbulence with a Compliant Surface. 53d Annual Meeting of The American Physical Society's Division of Fluid Dynamics, Washington, DC, November 2000. Contributed.
- V. Juttijudata, D. Rempfer, J. Lumley. Development of a Localized Low-Dimensional Approach to Turbulence Simulation. 53d Annual Meeting of The American Physical Society's Division of Fluid Dynamics, Washington, DC, November 2000. Contributed.

6.2 Technology Transitions or Transfer

None.

6.3 New Discoveries, Inventions, or Patent Disclosures

None.

6.4 Honors/Awards

John Lumley is a Fellow of the American Academy of Arts & Sciences, the American Physical Society, the American Academy of Mechanics, the American Institute of Aeronautics and Astronautics, and was a Guggenheim Fellow from 1973–74.

Dietmar Rempfer was supported by a Heisenberg Grant from the German National Science Foundation (Deutsche Forschungsgemeinschaft).

Sidney Leibovich is a Fellow of the American Academy of Arts & Sciences and the American Physical Society.

References

[1] AUBRY, N.; HOLMES, P.; LUMLEY, J. L.; STONE, E. (1988) The Dynamics of Coherent Structures in the Wall Region of a Turbulent Boundary Layer. *J. Fluid Mech.* **192**, pp. 115–173.

[2] BLOSSEY, P.; LUMLEY, J. L. (1998.) A low-dimensional approach to turbulence control in the minimal flow unit. *In preparation.*

[3] CHOI, K.-S.; YANG, X.; CLAYTON, B. R.; GLOVER, E. J.; ATLAR, M.; SEMENOV, B. N. & KULIK, V. M. (1997) Turbulent Drag Reduction Using Compliant Surfaces. *Proc. R. Soc. Lond. A* **453**, pp. 2229–2240.

[4] DAVIES, C.; CARPENTER, P. W. (1997) Numerical simulation of the evolution of Tollmien-Schlichting waves over finite compliant panels. *J. Fluid Mech.* **335**, pp. 361–392.

[5] HOLMES, P. J., LUMLEY, J. L. AND BERKOOZ, G. (1996)
Turbulence, Coherent Structures, Symmetry and Dynamical Systems. Cambridge, UK: University Press.

[Kang & Choi (2000)] KANG, S.; CHOI, H. 2000 Active wall motions for skin-friction drag reduction. *Phys. Fluids* **12**, 3301.

[6] MOHD-YUSOF, J. (1996) Interaction of Massive Particles with Turbulence. *PhD Thesis*, Cornell University.

[Semenov (1991)] SEMENOV, B. N. 1991 On conditions of modelling and choice of viscoelastic coatings for drag reduction. In: *Recent Developments in Turbulence Management*, (ed. K.-S. Choi), pp. 241-262.

[7] TOWNSEND, A. A. (1956) *Structure of Turbulent Shear Flows*, Cambridge University Press.